Composite 3D-printed metastructures for low-frequency and broadband vibration absorption

Kathryn H. Matlack[a,1], Anton Bauhofer[a], Sebastian Krödel[a], Antonio Palermo[a,b], and Chiara Daraio[a]

[a]Department of Mechanical and Process Engineering, ETH Zürich, 8092 Zurich, Switzerland; and [b]Department of Civil, Chemical, Environmental and Materials Engineering, University of Bologna, 40126 Bologna, Italy

Edited by Zhigang Suo, Harvard University, Cambridge, MA, and accepted by Editorial Board Member John A. Rogers June 6, 2016 (received for review January 6, 2016)

Architected materials that control elastic wave propagation are essential in vibration mitigation and sound attenuation. Phononic crystals and acoustic metamaterials use band-gap engineering to forbid certain frequencies from propagating through a material. However, existing solutions are limited in the low-frequency regimes and in their bandwidth of operation because they require impractical sizes and masses. Here, we present a class of materials (labeled elastic metastructures) that supports the formation of wide and low-frequency band gaps, while simultaneously reducing their global mass. To achieve these properties, the metastructures combine local resonances with structural modes of a periodic architected lattice. Whereas the band gaps in these metastructures are induced by Bragg scattering mechanisms, their key feature is that the band-gap size and frequency range can be controlled and broadened through local resonances, which are linked to changes in the lattice geometry. We demonstrate these principles experimentally, using advanced additive manufacturing methods, and inform our designs using finite-element simulations. This design strategy has a broad range of applications, including control of structural vibrations, noise, and shock mitigation.

metamaterials | phononic crystals | band gaps | 3D printing | vibration absorption

Architected materials exploit the geometry of their structure, which can be directly designed, to attain properties not common in bulk, continuum media. The underlying principles that determine the dynamic properties of architected materials are applicable across several length scales, and can be used to control phonons or elastic and acoustic waves, as in phononic crystals and acoustic metamaterials. In the linear regime, decreasing the size of the geometrical feature designed in the structure increases the operational frequency. This opens opportunities to control elastic/acoustic waves ranging from seismic excitations (hertz), structural vibrations (kilohertz), ultrasonic waves in microelectromechanical systems (MEMS) devices (megahertz), and thermal phonons in, e.g., thermoelectric materials (terahertz) (1–3).

Advanced manufacturing techniques, such as 3D printing, have progressed over size scales, ranging from meters down to nanometers. With these techniques, complex structures can be realized in many materials such as polymers, metals, and ceramics. Here, we design and test 3D-printed, composite materials, which combine a polymeric matrix with metallic components, and present a previously unidentified type of architected materials for broadband vibration mitigation.

Phononic crystals (PCs) consist of periodic arrangements of materials or components with controlled spatial sizes and elastic properties. When excited by an acoustic or elastic wave, PCs exhibit band gaps, or ranges of frequencies that cannot propagate through their bulk and decay exponentially. The band gaps in PCs arise from Bragg scattering mechanisms, and can be quite wide, making them desirable in sound mitigation and vibration absorption applications (4–8). However, the periodicity dimension and the material properties of the crystal's components limit the frequency range of band gaps found in PCs. These constraints limit the use of PCs in applications targeting low frequencies, because PCs would require impractically large geometries. To induce low-frequency band gaps, it is possible to design "metamaterials" that exploit locally resonant masses to absorb energy around their resonant frequency (9–12). However, band gaps in metamaterials are typically narrow-band in both acoustic (9, 13) and elastic wave attenuation applications (10, 14–16). Previous works have used concepts such as rainbow trapping effects (17), inertial amplification (8, 18), and combinations of phononic and locally resonant band gaps (19) to achieve wide and low-frequency band gaps.

Here, we introduce a different solution for opening low-frequency and wide band gaps: the coupling of local resonances with structural modes of an architected lattice, in what we refer to as "elastic metastructures." These metastructures are fundamentally different from metamaterials that incorporate resonators surrounded by a soft coating to induce low-frequency band gaps (9, 19), because our metastructures exploit the geometry of the structure instead of material properties to selectively alter different locally resonant modes. Further, these metastructures are not typical of traditional PCs because their band gaps can be tuned through local resonances. For concept validation, we design a 3D-printable elastic metastructure that combines characteristics of both metamaterials (i.e., local resonances) and PCs (i.e., periodicity), to achieve wide and low band gaps.

Unit Cell Design and Fabrication

The metastructures consist of a polycarbonate lattice, with embedded steel cubes acting as local resonators. The fundamental

Significance

Architected material used to control elastic wave propagation has thus far relied on two mechanisms for forming band gaps, or frequency ranges that cannot propagate: (*i*) Phononic crystals rely on their structural periodicity to form Bragg band gaps, but are limited in the low-frequency ranges because their unit cell size scales with wavelength; and (*ii*) Metamaterials overcome this size dependence because they rely on local resonances, but the resulting band gaps are very narrow. Here, we introduce a class of materials, elastic metastructures, that exploit resonating elements to broaden and lower Bragg gaps while reducing the mass of the system. This approach to band-gap engineering can be used for low-frequency vibration absorption and wave guiding across length scales.

Author contributions: K.H.M., A.B., and C.D. designed research; K.H.M., A.B., S.K., and A.P. performed research; K.H.M., A.B., A.P., and C.D. analyzed data; and K.H.M. and C.D. wrote the paper.

The authors declare no conflict of interest.

This article is a PNAS Direct Submission. Z.S. is a guest editor invited by the Editorial Board.

[1]To whom correspondence should be addressed. Email: matlackk@ethz.ch.

This article contains supporting information online at www.pnas.org/lookup/suppl/doi:10.1073/pnas.1600171113/-/DCSupplemental.

design components and the metastructure fabrication are shown in Fig. 1. The basic building block of our metastructures is a primitive cubic cell of polycarbonate (Fig. 1*A*). The unit cell is made of 12 beams of length L (3.65 mm) and thickness $t/2$ (0.55 mm). By tessellating this primitive cell in three dimensions, we create the periodic lattice, which serves as a structural support matrix. We consider volume elements composed of $5 \times 5 \times 5$ primitive cells as a mesoscale cell, with side length a (18.25 mm).

Metallic inclusions were embedded in the polycarbonate matrix to support the formation of low-frequency local resonances. To incorporate these inclusions, we embed steel cubes coated in a layer of polycarbonate, roughly the dimensions of $3 \times 3 \times 3$ primitive cells, inside the mesoscale cells (Fig. 1*B*). The metallic mass constitutes 11% volume fraction of each individual mesoscale cell. The complete metastructure is formed by creating a one-dimensional array of these cells (Fig. 1 *G* and *H*) along the x direction to effectively form an infinitely long beam. The presence of a periodic polymeric lattice, which functions as a matrix surrounding the metallic elements, enables direct control of the local resonances of the metastructure through small variations of the lattice geometry.

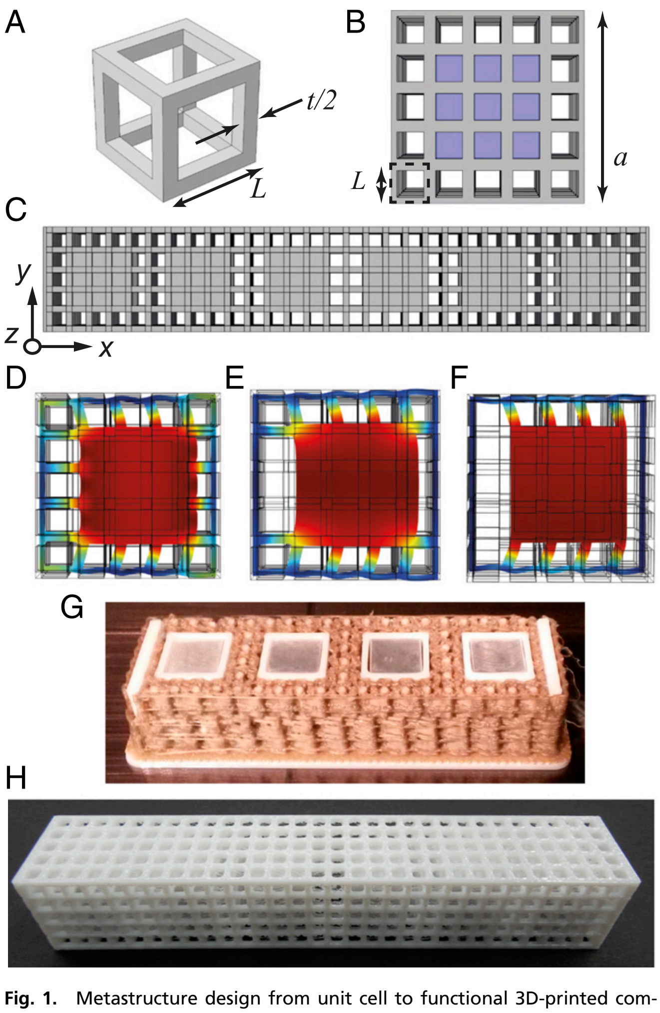

Fig. 1. Metastructure design from unit cell to functional 3D-printed component. (*A*) Primitive unit cell of the cubic lattice. (*B*) Mesoscale unit cell with embedded resonator (area in purple). The primitive unit cell is indicated by the dashed box. (*C*) One-dimensional chain of mesoscale unit cells with periodicity in the *x* direction. (*D*) High-stiffness, (*E*) mid-stiffness, and (*F*) low-stiffness metastructures, all shown with the modal displacement of the longitudinal locally resonant mode. (*G*) Photograph of a metastructure during 3D printing, with polycarbonate lattice (white), support material (brown), and embedded steel resonators (gray). (*H*) Final 3D-printed metastructure with embedded resonators.

We focus on three lattice designs: a high-stiffness metastructure and two modifications of this structure to form a mid-stiffness and low-stiffness metastructure. The high-stiffness metastructure is obtained using primitive unit cells to completely surround and embed in a structured matrix the steel resonators (Fig. 1*D*). The mid-stiffness and low-stiffness metastructures are designed to specifically lower the longitudinal locally resonant mode. The mid-stiffness metastructure is obtained by removing 24 horizontal beams from the resonator sides (Fig. 1*E*), from the initial high-stiffness geometry that contains 96 beams connected to the resonator sides. The low-stiffness metastructure is obtained by removing 32 horizontal beams from the initial high-stiffness geometry (Fig. 1*F*). These unit cell designs allow us to study how to use the lattice geometry to control the resonator modes, while maximizing the band-gap width (Fig. S1).

We fabricate samples using an advanced approach that combines 3D printing using fused deposition-modeling technology (using a Fortus 400mc 3D printer) with manual components assembling. To fabricate the metastructures, the polycarbonate lattice is 3D-printed up to the top of the steel cubes, including a void where the cubes will be placed. To insert the metallic cubes in the lattice, the 3D printer is paused immediately before printing the layer above the steel cubes, and the cubes are manually inserted into the part. A photograph of a metastructure midprint is shown in Fig. 1*G*. After completing the lattice printing, the sample is removed from the printing chamber and cooled, during which the polycarbonate lattice shrinks slightly, binding the steel cubes in place. Samples for testing are printed with six unit cells (Fig. 1*H*), which is sufficient to support the calculated band gaps. We tested the samples by exciting them with structural vibrations in the longitudinal direction and monitoring the transmission of elastic waves with accelerometers and force sensors (*Materials and Methods*, and *SI Materials and Methods*).

Controlling Local Resonances Through Geometry

Infinite Metastructures. The 1D dispersion relation of the high-stiffness metastructure, calculated using finite-element (FE) modeling (*Materials and Methods*), shows this metastructure supports a band gap with a center frequency of 7,454 Hz and normalized bandwidth of 27% (Fig. 2*A*). The lower-edge mode of the band gap is a combination of a longitudinal vibration of the embedded resonator, where the modal mass is primarily in the resonator that vibrates in the direction of periodicity, and a rotational mode of the resonator with a flexural motion of the surrounding lattice (Fig. 2 *A*, a4 and Fig. 1*D*). The upper edge mode (Fig. 2 *A*, a5) is a torsional mode.

Inspecting the edge mode shapes of the band gap in the high-stiffness metastructure gives an understanding of the fundamental mechanisms for band-gap formation. This allows us to identify the correct parameters to engineer lattices with wider band gaps at lower frequencies by controlling the locally resonant modes. In particular, variations of the lower-edge mode stiffness can "move" the mode toward desired frequency ranges, to engineer band gaps at lower frequencies. In the high-stiffness metastructure, the lower-edge mode is a longitudinal locally resonant mode, and its stiffness stems from the response of the beams connecting the metallic resonator to the surrounding lattice. Because the motion of the resonator in this mode is primarily in the x direction, the beams with axis along the x direction are under axial deformation, whereas the beams with axis in the y- or z direction are under bending deformation. Beams deform more easily in bending than in axial loading, so the axially loaded beams carry a significant portion of the stiffness of this mode. To design other metastructures that target this longitudinal locally resonant mode, we remove axially loaded beams from the mesoscale cells (Fig. 1 *E* and *F*). In the mid-stiffness metastructure, all axially loaded beams

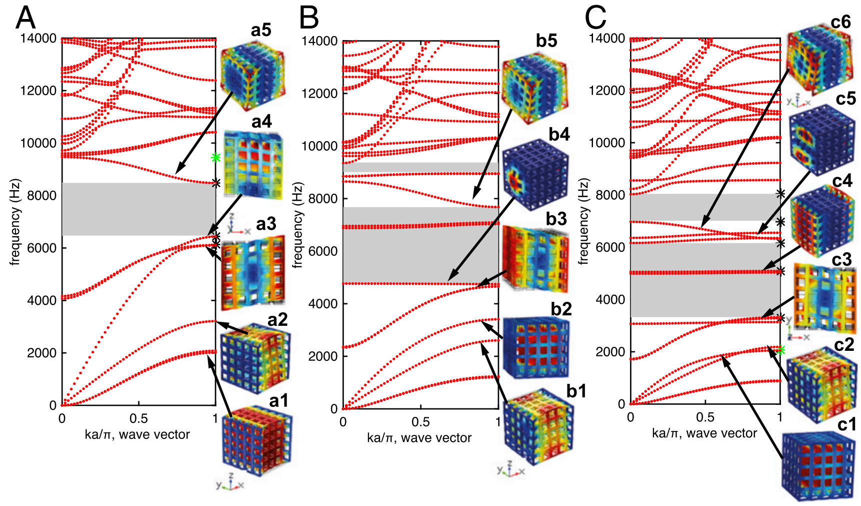

Fig. 2. Dispersion relations calculated with FE simulations for (*A*) the high-stiffness geometry, (*B*) the mid-stiffness geometry, and (*C*) the low-stiffness geometry. In *A*, *a1–a5*; *B*, *b1–b5*; and *C*, *c1–c6* the relevant mode shapes are plotted in terms of normalized modal displacements.

except the corner beams are removed from each unit cell—in total, 24 beams with length L and square cross-section with thickness t. In the low-stiffness metastructure, all axially loaded beams are removed from each unit cell—in total, 32 beams, corresponding to 1.6% of the structural mass.

The mid-stiffness metastructure shows a wider and lower band gap than the high-stiffness structure (Fig. 2*B*), with a center frequency of 6,212 Hz and bandwidth of 49%. The longitudinal mode (Fig. 2 *B*, *b2*) has dropped well below the second flexural mode (Fig. 2 *B*, b3), which now dictates the lower edge of the band gap. This change in mode order shows our ability to manipulate the locally resonant modes with geometry. The upper edge of the band gap is still the higher-order torsional mode (Fig. 2 *B*, *b5*) that has only decreased slightly in frequency. We were able to prevent this mode from decreasing in frequency through the unit cell design—the corner beams that remain on the mid-stiffness metastructure provide a significant portion of the stiffness of this lattice mode.

The low-stiffness metastructure supports an even lower and wider band gap (Fig. 2*C*), with a center frequency of 4,822 Hz with a normalized bandwidth of 62%. The lower edge of the band gap is the second flexural mode (Fig. 2 *C*, *c3*) that decreased further in frequency from the mid-stiffness metastructure, whereas the longitudinal mode (Fig. 2 *C*, *c1*) has also decreased further, even below the torsional resonant mode (Fig. 2 *C*, *c2*). Two modes containing pure lattice deformations reside within the band gap (Fig. 2 *C*, *c4*), but due to their near-zero group velocity they do not propagate and remain highly localized. It is clear that the removed beams had a strong contribution to the stiffness of the longitudinal mode, evident in the edge frequency reduction from 6,433 to 2,052 Hz from the high-stiffness to the low-stiffness metastructure. The removal of the beams also decoupled

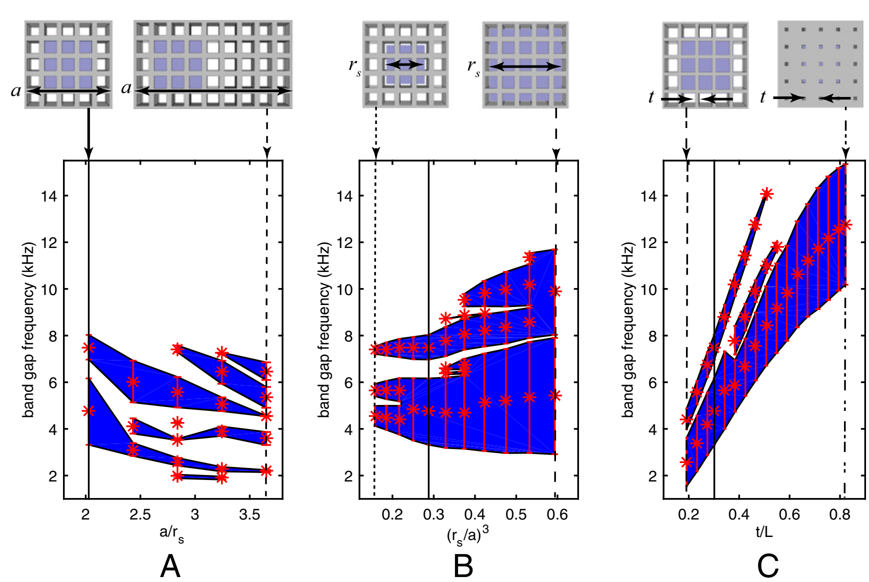

Fig. 3. Low-stiffness metastructure band-gap dependence on (*A*) unit cell size *a* with constant resonator size r_s (i.e., inverse of resonator packing density, r_s/a); (*B*) resonator filling fraction (constant unit cell size); and (*C*) beam thickness *t* normalized by beam length *L*. Data points indicate the band-gap center frequency; bars indicate bandwidth. Shaded regions indicate presence of band gaps, and the solid vertical line indicates the operational point of the 3D-printed low-stiffness metastructure. The unit cell designs are shown for the upper and lower bounds for each case.

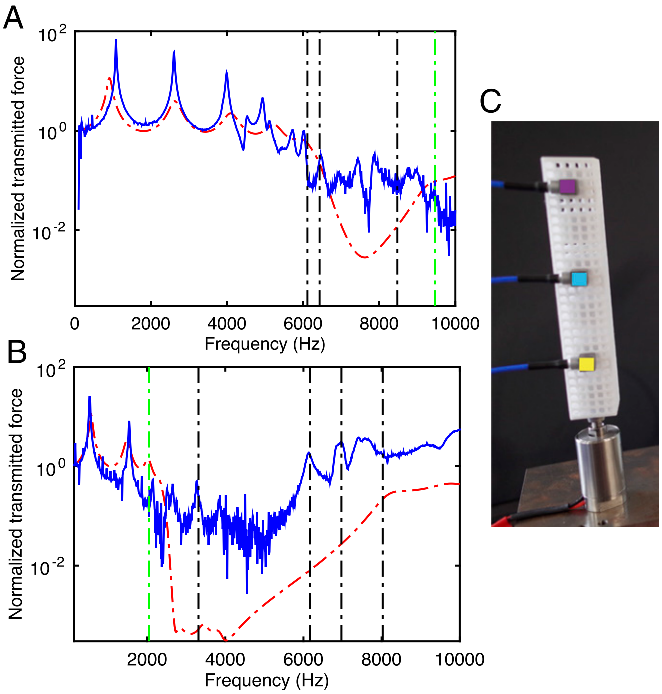

Fig. 4. FE simulation transmission (dashed red) through the six-unit cell metastructures and experimental results (solid blue) for the (*A*) high-stiffness and (*B*) low-stiffness metastructures. Results are individually normalized by the structural response at 100 Hz. Black vertical lines indicate band-gap edges calculated from the infinite metastructure dispersion relations, and green vertical lines indicate other modes in the dispersion dictating band gaps in the finite metastructures. Frequencies of these vertical lines are indicated as star data points in Fig. 2. (*C*) Photograph of experimental setup measuring acceleration along the metastructure length as shown in Movie S1.

the successive resonators, causing a decrease of the group velocity of the lower acoustic modes, as evident by the flatter bands toward the edge of the band structure. These numerical results show that we can significantly lower and widen the band gaps in these metastructures by tuning the local resonances through the manipulation of key geometrical parameters.

Design Flexibility. Further modifications to the metastructure geometry can result in widely different dispersion characteristics. Fig. 3 shows how tuning (*A*) the resonator packing density, (*B*) the resonator filling fraction, and (*C*) the thickness of the lattice beams can result in a variety of band-gap formations in the low-stiffness metastructure. For example, increasing the beam thickness with respect to beam length results in higher and narrower band gaps (Fig. 3*C*). Fig. 3*B* shows that the band-gap mechanism in these metastructures is not characteristic of typical Bragg scattering, where there is an intermediary filling fraction that yields the widest band gap (20). Fig. 3*A* shows the band gap is also not characteristic of the three-component locally resonant metamaterial concept where there is a monotonic increase of band-gap width with increasing resonator packing density, where the lower mode remains unchanged (21). When increasing the mesoscale size (i.e., decreasing the resonator packing density), the lower band gap decreases in frequency as shown in Fig. 3*A*, consistent with Bragg-scattering-induced band gaps. The increase in lattice volume also causes both localized modes within the band gap of the low-stiffness metastructure to turn into propagating modes, breaking up the band gap. These results illustrate the flexibility of a simple lattice design in terms of a variety of band-gap formations, and also shed light on the complexity of the character of the band gaps.

Finite Metastructures. The elastic wave transmission through six unit cell metastructures, similar to the experimental samples, was calculated with FE simulations (Fig. 4 *A* and *B*). Band gaps are evident between 6,000 and 9,500 Hz and between 2,040 and 8,360 Hz in the high- and low-stiffness metastructures, respectively. These results show quantitative agreement with the simulations of the infinite metastructures (Fig. 2 *A* and *C*), when taking into account that only x-direction motion is excited in the finite structures. Modes that do not have primary displacement in the x direction are not efficiently excited because the material is driven only in the x direction and thus do not play an important role in the dynamics of the finite structures, compared with the predictions obtained for an infinite system.

We experimentally tested finite metastructures in the high- and low-stiffness geometries (Fig. S2). Good agreement is seen between experiment and FE simulations in both the lower structural modes, as well as with the band-gap edges in both geometries (Fig. 4 *A* and *B*). Band gaps are measured between 6,020 and 10,000 Hz and between 2,150 and 6,110 Hz, in the high- and low-stiffness metastructure, respectively. Whereas experimental results show the presence of some high-frequency modes not observed in the finite-structure FE simulations, these peaks show good agreement with edge modes calculated in the dispersion relation for infinite structures. The presence of inconsistencies between the FE results and experiments may be due to small misalignments in the experimental setup, as well as not being able to experimentally excite modes with a negative group velocity, and are further discussed in *Supporting Information*.

Additional validation of the presence of band gaps in the experimental samples is shown in Movie S1 (also Fig. 4*C*), where the elastic wave response is measured at selected points along the length of the metastructure. The video clearly shows the wide band gap in the low-stiffness metastructure, where the measured responses approach zero, whereas the high-stiffness metastructure still supports elastic wave transmission.

It is evident that the numerical model is able to capture and predict the experimental response of the metastructures. This supports the design strategy in which informed changes to the lattice geometry can control locally resonant modes. This control results in experimentally verified lower and wider band gaps, while simultaneously decreasing the overall mass of the metastructure.

Band-Gap Mechanisms

To gain insight into the fundamental origin of the band gaps in the metastructures, we analyze the dispersion relation of the low-stiffness metastructure using a $\kappa(\omega)$ approach, to extract the complex dispersion relation (22). Band gaps induced by Bragg scattering, which is the mechanism responsible for band-gap formation in periodic media, contain evanescent modes within the band gap that connect nearby propagating modes with the same polarization/symmetry (22–24). For our beam metastructure, these different symmetries correspond to the families of flexural, torsional, and longitudinal modes. Band gaps that are induced by local resonances, on the other hand, exhibit sharp spikes in the complex wavenumber domain and can be identified by their asymmetric Fano profiles (25). The imaginary components of the wavenumber within the low-frequency band gap of the low-stiffness metastructure are indicative of Bragg scattering mechanisms (Fig. S3).

Further insight into the band-gap mechanism can be gained by a close inspection of the different wave modes in the dispersion relation. Bragg scattering causes band gaps to form at wavelengths around the lattice periodic constant of the structure, i.e., at a band-gap frequency of $f_{Bragg} = c/2a$, where c is the phase velocity in the medium. This predicted Bragg scattering frequency depends on the mode type considered for the effective properties. We determine effective phase velocities directly from the band structures using the relation $c = \omega/\kappa$ as κ approaches 0, for the lowest flexural, torsional, and longitudinal mode. This approximation, and the resulting flexural, torsional, and longitudinal band gaps, are shown in Figs. S4 and S5 for the high- and low-stiffness metastructures. It is shown that the Bragg scattering frequencies for each wave mode fall within the band gap calculated with FE simulations.

However, the resulting full band gaps observed in the metastructures are a superposition of the flexural, torsional, and longitudinal band gaps (Figs. S4–S6). By controlling the different wave modes independently, we can tune the full band gap to wider and lower frequency ranges, which we demonstrate by small manipulations of the lattice geometry to specifically control the band-gap edge modes.

Both FE simulations and experimental results of these proposed metastructures clearly show the ability to engineer low-frequency and wide band gaps by using the lattice geometry to selectively control the locally resonant modes. In addition, flexibility in the geometric design enables a variety of band-gap frequencies, distributions, and widths by varying the beam's thickness, the resonator and lattice dimensions, and filling fractions. With advanced 3D printing techniques, these metastructures could be fabricated on many different length scales to address a wide range of vibration isolation and wave-guiding applications, ranging from structural vibrations to MEMS devices.

Materials and Methods

FE Simulations. FE simulations (COMSOL) in 3D are used to analyze the infinite and finite metastructures. For the infinite metastructure simulations, a single unit cell was modeled and periodic Bloch boundary conditions were imposed. An eigenfrequency analysis was performed by sweeping the wave vector over the reduced Brillouin zone. We used tetrahedral elements, and mesh convergence was confirmed.

For the finite metastructure simulations, the elastic wave transmission was calculated by imposing a fixed boundary on one end of the six-unit cell chain, and measuring the reaction force on the opposite end. The transmission was defined as the ratio of output to input force amplitudes, and was calculated over a range of frequencies from 100 to 10,000 Hz (Fig. 4). The results shown are based on a harmonic x-direction displacement input. Band-gap edge frequencies calculated for the infinite system are indicated as dashed vertical lines in the same plots.

Parameters of 3D-Printed Materials. The material properties and key geometrical parameters used in the simulations are given in Tables S1 and S2. The Young's modulus used for the 3D-printed polycarbonate was measured through tensile testing on 3D-printed standard tensile testing samples with different printing orientations, to account for anisotropy in the 3D-printed polycarbonate. Because 3D-printed material is known to be highly dependent on specific printing parameters, the measured Young's modulus was further tuned such that the low-frequency mode in the finite FE simulations aligned with the low-frequency mode in the dynamic experiments presented in Fig. 4. The shear modulus was calculated based on a Poisson's ratio of 0.4 (27).

It is well known that 3D-printed materials can have anisotropic mechanical properties that are dependent on the printing geometry, orientation, and ambient conditions (26). Our FE model assumes the lattice materials to be homogeneous and slightly anisotropic. As such, parameter-dependent deviations between experiments and simulations are also to be expected.

Experiments. To experimentally measure the elastic wave transmission through the metastructures, we fix the 3D-printed samples between a piezo actuator and a force sensor, which respectively excite and measure x-direction motion of the structure. A lock-in amplifier drives the piezo actuator and measures the response of the structure. A static load cell continuously monitors the precompression of the structure during experiments (due to the sample's supports) to ensure consistent boundary conditions when mounting different samples. The experiments presented in Fig. 4 *A* and *B* measured output force. The setup is shown in Fig. S2, consisting of a fixed static load cell mounted against a dynamic force sensor on a frictionless support, and a piezo actuator mounted on movable support to control precompression of the sample. To confirm a flat response of the system over the frequency range of interest (1–10 kHz), the response of the system without a sample was measured by pressing the force sensor against the piezo actuator, with the same precompression as in the transmission experiments. The noise floor in the experimental setup can be seen in the band gaps of both structures (Fig. 4).

For the experiments shown in Movie S1, accelerometers were glued to the exterior of the high- and low-stiffness metastructures, at heights corresponding to the second, fourth, and sixth resonator. The accelerometers measured the acceleration in the vertical direction, which is the direction of periodicity. The metastructures were mounted on a piezo actuator, which was swept in frequency from 1 to 6.5 kHz over about 25 s. The waveforms shown are the responses of the top (purple), middle (blue), and bottom (yellow) accelerometers. The transmission spectrum at the bottom of the screen shows the finite simulation results for both high- and low-stiffness metastructures, and the solid vertical line shows the swept frequency corresponding to the experimental sweep. The waveforms are recorded directly from a Tektronix DPO 3034 oscilloscope and are recorded at the same scale such that the amplitudes of the high- and low-stiffness metastructre responses are directly comparable.

ACKNOWLEDGMENTS. The authors acknowledge Shi En Kim for performing the measurements of the 3D-printed material properties. This work was partially supported by the ETH Postdoctoral Fellowship to K.H.M., and partially supported by the Swiss National Science Foundation Grant 164375.

1. Maldovan M (2013) Sound and heat revolutions in phononics. *Nature* 503(7475): 209–217.
2. Li N, et al. (2012) Colloquium: Phononics: Manipulating heat flow with electronic analogs and beyond. *Rev Mod Phys* 84(3):1045–1066.
3. Yang L, Yang N, Li B (2014) Extreme low thermal conductivity in nanoscale 3D Si phononic crystal with spherical pores. *Nano Lett* 14(4):1734–1738.
4. Hsu FC, et al. (2010) Acoustic band gaps in phononic crystal strip waveguides. *Appl Phys Lett* 96(051902):2008–2011.
5. Wang L, Bertoldi K (2012) Mechanically tunable phononic band gaps in three-dimensional periodic elastomeric structures. *Int J Solids Struct* 49(19-20):2881–2885.
6. Bilal OR, Hussein MI (2011) Ultrawide phononic band gap for combined in-plane and out-of-plane waves. *Phys Rev E Stat Nonlin Soft Matter Phys* 84(6 Pt 2):065701.
7. Martin A, Kadic M, Schittny R, Bückmann T, Wegener M (2012) Phonon band structures of three-dimensional pentamode metamaterials. *Phys Rev B* 86(15):155116.
8. Yilmaz C, Hulbert G, Kikuchi N (2007) Phononic band gaps induced by inertial amplification in periodic media. *Phys Rev B* 76(5):054309.
9. Liu Z, et al. (2000) Locally resonant sonic materials. *Science* 289(5485):1734–1736.
10. Baravelli E, Ruzzene M (2013) Internally resonating lattices for bandgap generation and low-frequency vibration control. *J Sound Vib* 332(25):6562–6579.
11. Bonanomi L, Theocharis G, Daraio C (2015) Wave propagation in granular chains with local resonances. *Phys Rev E Stat Nonlin Soft Matter Phys* 91(3):033208.
12. Khelif A, Achaoui Y, Benchabane S, Laude V, Aoubiza B (2010) Locally resonant surface acoustic wave band gaps in a two-dimensional phononic crystal of pillars on a surface. *Phys Rev B* 81(214303):1–7.
13. Fang N, et al. (2006) Ultrasonic metamaterials with negative modulus. *Nat Mater* 5(6): 452–456.
14. Zhu R, Liu XN, Hu GK, Sun CT, Huang GL (2014) A chiral elastic metamaterial beam for broadband vibration suppression. *J Sound Vib* 333(10):2759–2773.
15. Liu XN, Hu GK, Sun CT, Huang GL (2011) Wave propagation characterization and design of two-dimensional elastic chiral metacomposite. *J Sound Vib* 330(11):2536–2553.
16. Nouh M, Aldraihem O, Baz A (2014) Vibration characteristics of metamaterial beams with periodic local resonances. *J Vib Acoust* 136(6):061012.
17. Krödel S, Thomé N, Daraio C (2015) Wide band-gap seismic metastructures. *Extreme Mech Lett* 4(September):111–117.
18. Taniker S, Yilmaz C (2013) Phononic gaps induced by inertial amplification in BCC and FCC lattices. *Phys Lett A* 377(31-33):1930–1936.
19. Yuan B, Humphrey VF, Wen J, Wen X (2013) On the coupling of resonance and Bragg scattering effects in three-dimensional locally resonant sonic materials. *Ultrasonics* 53(7):1332–1343.
20. Goffaux C, Sanchez-Dehesa J (2003) Two-dimensional phononic crystals studied using a variational method: Application to lattices of locally resonant materials. *Phys Rev B* 67:144301.
21. Liu Z, Chan C, Sheng P (2002) Three-component elastic wave band-gap material. *Phys Rev B* 65:165116.
22. Veres IA, Berer T, Matsuda O (2013) Complex band structures of two dimensional phononic crystals: Analysis by the finite element method. *J Appl Phys* 114:083519.
23. Romero-Garcia V, Sánchez-Perez JV, Garcia-Raffi LM (2010) Evanescent modes in sonic crystals: Complex dispersion relation and supercell approximation. *J Appl Phys* 108(4):044907.
24. Laude V, Achaoui Y, Benchabane S, Khelif A (2009) Evanescent Bloch waves and the complex band structure of phononic crystals. *Phys Rev B* 80(092301):1–4.
25. Goffaux C, et al. (2002) Evidence of Fano-like interference phenomena in locally resonant materials. *Phys Rev Lett* 88(22):225502.
26. Mueller J, Shea K, Daraio C (2015) Mechanical properties of parts fabricated with inkjet 3D printing through efficient experimental design. *Mater Des* 86:902–912.
27. Mazeran PE, et al. (2012) Determination of mechanical properties by nano-indentation in the case of viscous materials. *Int J Mat Res* 103(6):715–722.